Virtual Antenna Array for W-band Channel Sounding

Design, Implementation, and Experimental Validation

Lyu, Yejian; Yuan, Zhiqiang; Zhang, Fengchun; Kyösti, Pekka; Fan, Wei

Published in:
I E E E Journal on Selected Topics in Signal Processing

DOI (link to publication from Publisher):
10.1109/JSTSP.2023.3301135

Publication date:
2023

Document Version
Accepted author manuscript, peer reviewed version

Virtual Antenna Array for W-band Channel Sounding: Design, Implementation, and Experimental Validation

Yejian Lyu, Zhiqiang Yuan, Fengchun Zhang, Pekka Kyösti, and Wei Fan

***Abstract*—Sub-Terahertz (sub-THz) (i.e., 100-300 GHz) communication is envisioned as one of the key components for future beyond fifth-generation (B5G) communication systems due to its large untapped bandwidth. Sub-THz channel measurements are essential for building accurate and realistic sub-THz channel models. Virtual antenna array (VAA) scheme has been widely employed for radio channel sounding purposes in the literature. However, its application for the W-band (i.e., 75-110 GHz) has been rarely discussed due to system phase instability issues. To tackle this problem, a long-range phase-compensated vector network analyzer (VNA)-based channel sounder at the W-band is proposed. First, the back-to-back measurement of the developed channel sounder is carried out with the presence of cable bending, where the initial phase variation beyond 180° range due to cable effects can be well corrected to within 10° range with the proposed phase-compensation scheme, clearly validating its effectiveness. To examine how well it works in practical deployment scenarios, the proposed channel sounder is then employed for channel sounding with two measurement distances, covering both near-field (with a line-of-sight (LoS) distance of 7.3 m) and long-range (with a LoS distance of 84.5 m) cases. Based on the measured data, a high-resolution channel parameter estimator is applied to extract the channel multipath parameters for the large-scale VAA at the W-band, both in the near-field and long-range scenarios, respectively. The high-resolution algorithm was extended to support virtual arrays composed of both omnidirectional antenna and directive antenna in this work. The conventional directional scanning scheme (DSS) measurement is adopted as the reference measurement to validate the effectiveness and robustness of the developed channel sounder. In the end, to demonstrate the state-of-art channel sounding capabilities of the developed channel sounder, ultra-wideband (UWB) channel measurements at 104.5 GHz with 11 GHz bandwidth using the VAA scheme are conducted in a hall scenario with the measurement range up to 58 m with omnidirectional antennas, and the channel parameters are extracted using the validated high-resolution channel parameter estimator for channel modeling purposes.**

***Index Terms*—Channel sounding, sub-terahertz, virtual antenna array, channel modeling, high-resolution multipath extraction algorithm.**

I. Introduction

With the maturation and commercialization of fifth-generation (5G) communications, research on next-generation communications, i.e., Beyond 5G, has been gaining momentum recently [1], [2]. Sub-terahertz (sub-THz) frequencies ranging from 100 to 300 GHz are expected to be a key component for next-generation communication systems, providing huge unregulated and untapped bandwidth [3]–[5]. There has been a strong research focus on sub-THz communications in recent years, with strong efforts taken by the government, research institutes, standardization, and industries [6]–[8].

Channel modeling is crucial for system design and performance evaluation for future communication systems. Accurate channel modeling relies on high-fidelity channel data collected by the experimental platform, i.e., the channel sounder, in typical deployment scenarios. However, there are still many issues with channel sounder design and measurements in sub-THz frequencies. Vector network analyzer (VNA)-based channel sounder is a popular channel sounder to measure sub-THz channels, thanks to its unique advantages, e.g., easy calibration, flexible carrier frequency and bandwidth settings, and high system dynamic range [9]–[11]. The VNA is by default a frequency domain channel sounder that houses a signal generator and analyzer internally, which makes phase and frequency synchronization easy to implement [12]. However, the VNA needs coaxial cables to connect and remote the transmitting and the receiving antennas to support measurements over distance. However, the signal transmission over coaxial cables suffers from large cable loss at higher frequencies, especially at sub-THz frequencies, leading to a significantly reduced dynamic range. The radio-over-fiber (RoF) technique which up-converts the electrical signal to the optical signal and then transmits it through the optical fiber, can greatly reduce the cable loss (e.g. as low as 0.4 dB/km with a high-quality signal mode fiber, compared to 1.75 dB/m at 15 GHz with a typical coaxial cable [13]), making it possible to support long-range measurements.

Knowledge of channel spatial profile is of high importance, especially for millimeter-wave (mmWave) and sub-THz radios where beam-tracking is essential to maintain the communication link in dynamic scenarios. Directional scanning scheme (DSS) is a popular method to obtain channel spatial information at sub-THz bands due to its simplicity and low-cost [27]–[29]. The basic idea is that a directive antenna is placed and mechanically rotated in the center of a turntable at the transmitter (Tx) and/or receiver (Rx), and

Y. Lyu, F. Zhang, and W. Fan are with the Antenna, Propagation and Millimeter-wave Systems (APMS) Section, Department of Electronic Systems, Faculty of Engineering and Science, Aalborg University, 9220 Aalborg, Denmark (e-mail: yely@es.aau.dk; fz@es.aau.dk; wfa@es.aau.dk);

Z. Yuan is with the State Key Lab of Networking and Switching Technology, Beijing University of Posts and Telecommunications, 100876 Beijing, China, and also with APMS Section, Aalborg University, 9220 Aalborg, Denmark (e-mail: yuanzhiqiang@bupt.edu.cn).

P. Kyösti is with Oulu University and also with Keysight Technologies Finland Oy, Oulu 90630, Finland.

Corresponding author: Wei Fan.

TABLE I: Recent studies on VAA channel measurements.

Reference	Year	Frequency	VAA type	Scenario and Tx-Rx distance
[14]	2012	5.15-5.35 GHz	10×25 uniform rectangular array (URA)	Outdoor, up to 300 m
[15]	2010	2-8 GHz	Uniform circular array (UCA) with 97 elements	Indoor building, up to 35 m
[16]	2018	1.89 & 2.35 GHz	3-element uniform linear array (ULA)	Viaduct and railway
[17]	2014	60-64 GHz	7×7 URA	Conference room, within 6 m
[18]	2015	57.68-59.68 GHz	$25 \times 25 \times 25$ cubic array	Indoor office, 1.5 m
[19]	2016	28 GHz with 500 MHz bandwidth	UCA with 1600 elements	Hall, 14 m
[20]	2020	26-30 GHz	21×21 URA	Lab, 4-5.2 m
[21]	2022	12-14 GHz	32×32 URA	Meeting room, 7.2 m
[22]	2022	26.5-40 GHz	35×35 URA	Industrial scenario & Meeting room
[23]	2022	27.9-28.1 GHz	3D array with 37 elements	Anechoic chamber
[24]	2020	26.5-30 GHz	30×30 URA	Hall, 46 m
[25]	2022	28-30 GHz	UCA with 240 elements	Corridor, 11.4-33.4 m
[26]	2022	99-101 GHz	UCA with 360 elements	Corridor, 20 m

channel impulse response (CIR) for each rotated direction is recorded. However, the spatial resolution is limited by the directivity of the employed antennas. Another widely applied channel sounding scheme is based on virtual antenna arrays (VAAs), where a single antenna is moved to multiple spatial locations, and the CIR at each spatial location (i.e. virtual array antenna element) is sequentially recorded [30], [31]. By using the appropriate array processing algorithm, e.g., beamforming and maximum likelihood estimation algorithms, the VAA can achieve a high spatial resolution. A list of representative VAA works in the state-of-art works in recent years is summarized in Table I. VAA scheme has been widely adopted in the channel measurements at sub-6 GHz bands, with various measurement distances thanks to the high phase accuracy and the low signal loss in the radio frequency (RF) coaxial cables [14]–[16]. Moving to mmWave bands, the VNA-based channel measurement suffers from high propagation loss in the channel and high attenuation in the coaxial cables, limiting the measurement mainly in the short-range scenarios, e.g. office and meeting room [17]–[22]. The performance of the VAA-based channel sounder highly relies on stable and accurate phase measurements, which is much more challenging in mmWave and sub-THz bands. It was explained in [8], [26] that the phase is unstable and sensitive to RF and mechanical stability of the system both in the conventional VNA-based channel sounder and RoF-enabled channel sounder at sub-THz. The phase-compensation scheme proposed in [13] can effectively mitigate the unstable phase problem in the channel sounder. The feasibility of the phase-compensation scheme for phase-coherent measurements at 220-330 GHz frequency bands was demonstrated in the back-to-back measurements in [13]. However, no real channel measurements were reported. In our previous magazine [26], we introduced the concept of the phase-compensated VNA-based channel sounder for sub-6GHz, mmWave, and sub-THz bands, however, technical details were not provided. Additionally, only the classical beamforming algorithm was used in [26], which restricts its application to narrowband far-field scenarios. Therefore, VAA channel sounder design, implementation, and experimental validation at the W-band are currently lacking in the literature, to the best knowledge of the authors. Furthermore, the development of a generic high-resolution multipath extraction algorithm for W-band channel measurements has not been reported, mainly due to the lack of an accurate phase-coherent experimental platform.

In this paper, we aim to fill this knowledge gap by proposing a phase-compensated RoF-enabled VNA-based channel sounder at the W-band, i.e., 75-110 GHz. The phase issue in the channel sounding system at sub-THz bands is first described and measured in the back-to-back connection. The simulated beamforming results without phase compensation are evaluated and compared with the reference results based on the empirical phase changes. After the evaluation of the phase change impact, a phase-compensated VNA-based channel sounder is proposed at W-bands and validated in the back-to-back connection. Besides, the VAA-based channel measurement campaign is conducted in a hall scenario at 100 GHz with two distances, i.e., near-field (7.3 m) and long-range (84.5 m). A high-resolution channel parameter estimator, i.e., frequency-invariant beamforming (FIBF) with successive interference cancellation (SIC) is employed to extract the parameters of the paths. The FIBF algorithm is also generalized for a UCA composed of any type of antenna element, for instance, the omnidirectional antenna (which has been reported in the literature) and directive antenna (proposed in this work). The estimation results obtained with both omnidirectional antenna-based VAA (Omni-VAA) and Dir-VAA are then validated by comparing the multi-path parameters with the reference DSS results. Readers can refer to [26] for detailed descriptions of the channel spatial profile measurement method, i.e., Omni-VAA, Dir-VAA, and DSS. Furthermore, to demonstrate the capability of the developed channel sounder, channel measurements covering near-field, long-range, and ultra-wideband scenarios were performed, and the channel characteristics in a hall scenario for the Tx-Rx distance varying within the range of $[3, 58]$ m are calculated and analyzed.

The main contributions of this paper are summarized as follows:

- The phase issues of the conventional VNA-based channel sounder using the RoF scheme is investigated. The impact of the phase instability issue of the channel sounder is then evaluated in a simulation.
- The phase-compensated VNA-based channel sounder at 75-110 GHz is designed and validated in the back-to-back connection. Thanks to the accurate complex signal measurement (i.e. both amplitude and phase) at each array element (i.e. spatial location) of the VAA channel measurement at the W-band, a high-resolution channel

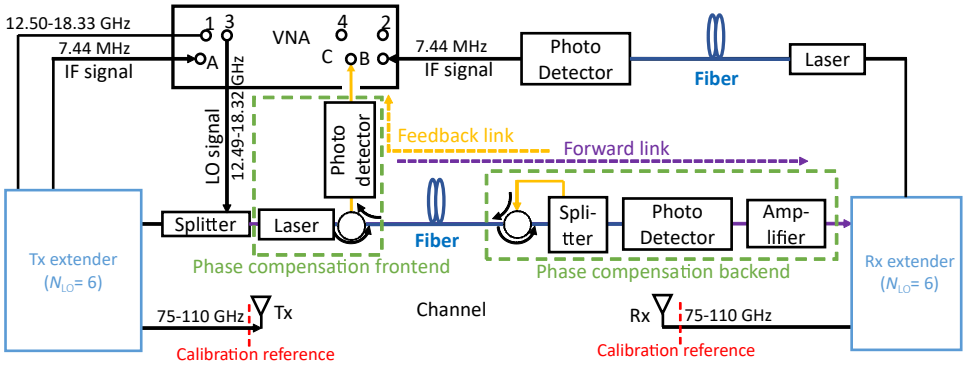

Fig. 1: Block diagram of the proposed phase-compensated VNA-based channel sounder at 100 GHz.

parameter estimator is enabled to extract the multipath parameters from the VAA channel measurements at the W-band, which has not been achieved in the state-of-the-art.

- The FIBF with the SIC algorithm was implemented for omnidirectional antennas in our previous work at mmWave bands. However, due to their low antenna gain, omnidirectional antennas are getting less popular as the frequency goes up. We generalize the FIBF algorithm to support both Omni-VAA, i.e. virtual array composed of omnidirectional elements, and Dir-VAA, i.e. composed of directive elements, and then validate the algorithm using the measurement results.
- Long-range VAA channel sounder in the W-band, enabled by the RoF and phase-compensation scheme is presented and validated, by comparing with the DSS measurement at W-bands with two measurement distances, i.e., near-field (with a line-of-sight (LoS) distance of 7.3 m) and far-field (with an LoS distance of 84.5 m).
- Ultra-wideband (UWB) omnidirectional VAA measurements at 99-110 GHz with 11 GHz bandwidth were performed at the Tx-Rx distances of 3-58 m. The channel parameters are analyzed using the high-resolution channel parameter estimator, and the channel characteristics, including path loss, delay spread, angular spread, and k-factor, are given.

The rest of this paper is organized as follows: Section II outlines the principle and the architecture of the proposed phase-compensation scheme. The high-resolution channel parameter estimator is described in Section III. Section IV contains the back-to-back validation measurements and the analysis of the results. Section V presents the over-the-air channel measurement validations at W-bands. Finally, concluding remarks are presented in Section VI.

II. Proposed Channel Sounder Architecture

A. Sounder Architecture

Fig. 1 depicts the proposed long-range phase-compensated VNA-based channel sounder at the W-band. The VNA is set to transmit the input signal in the frequency range of 12.50-18.33 GHz from port 1 and the local oscillator (LO) signal in the frequency range of 12.49-18.32 GHz from port 3, respectively. The input signal is up-converted to the frequency range of 75-110 GHz and transmitted through the Tx antenna. The LO signal is split by a splitter and multiplied by a factor of $N_{\mathrm{LO}} = 6$ for down-converting the RF signal to the IF signal at 7.44 MHz. The down-converted IF signals at the Tx and Rx sides are then recorded in port A and port B, respectively.

The RoF scheme and phase-compensation scheme are applied in the LO cable at the Rx side to extend the Rx for long-range measurement purposes, and to stabilize the phase change during the measurements, as shown in Fig. 1. At sub-6 GHz and mmWave bands, the phase compensation scheme can be directly employed to RF cable [24], [32]. However, due to the lack of such cost-effective electrical-to-optical (E/O) and optical-to-electrical (O/E) units at sub-THz bands, we cannot directly apply the phase-compensation scheme to the sub-THz channel sounder. Instead, thanks to the introduction of the frequency extenders, the phase-compensation scheme can be applied in the LO cable at the Rx side. The principle of the phase compensation scheme is that the optical circulators and splitter are used to construct a feedback link to record the phase change of the signal. Note that the phase change is mainly caused by the thermal change and mechanical stress in the fibers, which change the physical structure or properties of the fibers [33], [34]. The recorded feedback signal suffers twice the same phase change due to the mechanical stress and thermal change through the bidirectional fiber.

B. Principle of the Phase Compensation Concept

As depicted in Fig. 1, the forward link and feedback link are recorded in the VNA as the S-parameter $S_{\mathrm{BA}}(\mathbf{f_1})$ and $S_{\mathrm{C3}}(\mathbf{f_2})$, respectively, where we have $\mathbf{f_1} = [7.44, 7.44, \ldots, 7.44]$ MHz with N_1 frequency points, and $\mathbf{f_2} = [12.49, \ldots, 18.32]$ GHz with the same number of frequency points N_1. In over-the-air channel measurements with antennas, the recorded $S_{\mathrm{BA}}(\mathbf{f_1})$ can be expressed as:

$$S_{\mathrm{BA}}(\mathbf{f_1}) = H_{\mathrm{sys}}(\mathbf{f_1}) \cdot H(\mathbf{f_1}), \tag{1}$$

where $H_{\mathrm{sys}}(\mathbf{f_1})$ represents the system response including the mechanical stress and thermal change of the optical fiber cable, and $H(\mathbf{f_1})$ is the channel frequency response (CFR) including both the Tx and Rx antenna responses.

The frequency response in the feedback link $H_{\mathrm{fb}}(\mathbf{f_2})$, which records the error response of the optical fiber, is encoded in $S_{\mathrm{C3}}(\mathbf{f_2})$ as follows:

$$H_{\mathrm{fb}}(\mathbf{f_2}) = S_{\mathrm{C3}}(\mathbf{f_2}) = \alpha_{\mathrm{C3}}(\mathbf{f_2}) \exp(j\phi_{\mathrm{C3}}(\mathbf{f_2})), \tag{2}$$

where $\alpha_{\mathrm{C3}}(\mathbf{f_2})$ and $\phi_{\mathrm{C3}}(\mathbf{f_2})$ are the amplitude and phase of $S_{\mathrm{C3}}(\mathbf{f_2})$, respectively.

As explained in [13], [24], the signal experiences phase drift twice in the feedback link compared to the LO signal. Thus, the amplitude response $\alpha_{\mathrm{LO3}}(\mathbf{f_2})$ and phase response $\phi_{\mathrm{LO3}}(\mathbf{f_2})$ from the LO signal input port to Port 3 can be calculated as:

$$\alpha_{\mathrm{LO3}}(\mathbf{f_2}) = \sqrt{\alpha_{\mathrm{C3}}(\mathbf{f_2})} = \sqrt{|S_{\mathrm{C3}}(\mathbf{f_2})|}, \tag{3}$$

$$\phi_{\mathrm{LO3}}(\mathbf{f_2}) = \frac{\phi_{\mathrm{C3}}(\mathbf{f_2})}{2}, \tag{4}$$

where we assume that the amplifier in the LO cable side and the Rx extender are stable during the measurements. Thus, after passing through the $6\times$ multiplier and mixer, the amplitude $\alpha_{\mathrm{sys}}(\mathbf{f_1})$ and phase $\phi_{\mathrm{sys}}(\mathbf{f_1})$ of the error term $H_{\mathrm{sys}}(\mathbf{f_1})$ can be written as:

$$H_{\mathrm{sys}}(\mathbf{f_1}) = \sqrt{|S_{\mathrm{C3}}(\mathbf{f_2})|} \cdot \exp(j \cdot 3 \cdot \phi_{\mathrm{C3}}(\mathbf{f_2})). \tag{5}$$

As a result, we can remove the system response $H_{\mathrm{sys}}(\mathbf{f_1})$, which includes the undesired cable effects, from the recorded $S_{\mathrm{BA}}(\mathbf{f_1})$ and obtain $H(\mathbf{f_1})$:

$$\begin{aligned} H(\mathbf{f_1}) &= \frac{S_{\mathrm{BA}}(\mathbf{f_1})}{H_{\mathrm{sys}}(\mathbf{f_1})} \\ &= \frac{S_{\mathrm{BA}}(\mathbf{f_1})}{\sqrt{|S_{\mathrm{C3}}(\mathbf{f_2})|} \exp(j \cdot 3 \cdot \phi_{\mathrm{C3}}(\mathbf{f_2}))}. \end{aligned} \tag{6}$$

After performing the above compensation procedure, the phase errors introduced by the cable bending and thermal change of the optical fiber cable can be well calibrated.

III. High Resolution Parameter Estimator

A. Channel Parameter Estimator

The FIBF algorithm [35] is employed in this work to obtain the spatial channel profiles. It is a generic algorithm, which is demonstrated to work for small/large-scale and far/near-field UCA-based channel measurements in mmWave frequency bands. However, its application at sub-THz has not been reported in the literature due to the lack of available VAA measurement data in sub-THz bands. To compensate for the high path loss at mmWave and sub-THz bands, it is beneficial to employ high-gain directive antennas for increasing the dynamic range. Thus, in this study, we further generalize the FIBF algorithm to work for UCAs with any type of antenna element. The algorithm becomes applicable for a wider range of propagation scenarios, including both far-field and near-field, as well as both wideband and narrowband scenarios, regardingless of using omni-VAA or Dir-VAA configurations.

Assuming that the number of array elements and the number of paths are K and L, respectively. The radius of the UCA is r and the angular position of the k-th element is $\varphi_k = 2\pi(k-1)/K$. The ℓ-th path parameter set is denoted as:

$$\Theta_\ell = [\alpha_\ell, \tau_\ell, \phi_\ell], \tag{7}$$

where α_ℓ, τ_ℓ, and ϕ_ℓ represent the amplitude, delay, azimuth angle of the ℓ-th path, respectively. Note that other path parameters, e.g. elevation angle θ_ℓ and distance d_ℓ between the scatterer to the array center can be further estimated using maximum likelihood algorithms once we have obtained the key channel parameters in (7).

The CFR at the k-th antenna element of the UCA is:

$$H_k(f) = \sum_{\ell=1}^{L} \alpha_\ell \exp(-j2\pi f \tau_\ell) \cdot a_k(f, \phi_\ell), \tag{8}$$

where $a_k(f, \phi_\ell)$ is the array manifold coefficient of the kth array element of the ℓth path as:

$$a_k(f, \phi_\ell) = \frac{d_\ell}{d_{k,\ell}} \exp(-j2\pi f \Delta d_{k,\ell}/c) \cdot \Phi(f, \phi_\ell - \varphi_k). \tag{9}$$

$d_{k,\ell}$ and $\Phi(f, \phi_\ell - \varphi_k)$ denote the distance from the ℓ-th scatterer to the k-th UCA element and the complex antenna pattern of the antenna element (the pattern can be omnidirectional or directive), respectively. $\Delta d_{k,\ell}$ presents the difference between d_ℓ and $d_{k,\ell}$, which is written as:

$$\Delta d_{k,\ell} = d_\ell - d_{k,\ell}, \tag{10}$$

with

$$d_{k,\ell} = \sqrt{d_\ell^2 + r^2 - 2r d_\ell sin(\theta_\ell) cos(\phi_\ell - \varphi_k)}. \tag{11}$$

In the near-field case, we cannot directly use the classical beamforming algorithm based on the plane wave assumption [36], [37], due to the model mismatch error introduced in the near-field case. Thus, in this work, we use the FIBF algorithm for channel parameter estimation.

In the FIBF algorithm, we first transform the frequency response from the element domain (spatial domain) to the phase mode domain:

$$\begin{aligned} \widetilde{H}_m(f) &= \sum_{k=1}^{K} G_m(f) \cdot H_k(f) \cdot e^{jm\varphi_k} \\ &= \sum_{\ell=1}^{L} \alpha_\ell e^{-j2\pi f \tau_\ell} \cdot a_m(f, \phi_\ell), \end{aligned} \tag{12}$$

where $\widetilde{H}_m(f)$ and $G_m(f)$ denote the m-th mode response of the array in the phase mode domain and the compensation filter, respectively. The array manifold term in phase mode domain $a_m(f, d_\ell, \phi_\ell)$ is:

$$a_m(f, \phi_\ell) = \sum_{k=1}^{K} G_m(f) \cdot \exp(jm\phi_k) \cdot a_k(f, \phi_\ell). \tag{13}$$

The compensation filter $G_m(f)$ can be written as [35]:

$$G_m(f) = \frac{2}{j^m (J_m(2\pi f r/c) + J_m'(2\pi f r/c))}, \tag{14}$$

where $J_m(\cdot)$ is the Bessel function of the first kind with order m, and $(\cdot)'$ represents the differential operator.

Thus, the FIBF's beam pattern with array pattern de-embedded is obtained as follows:

$$B(f, \phi) = \frac{1}{T(f)} \sum_{m=-M}^{M} \exp(-jm\phi) \cdot \widetilde{H}_m(f), \tag{15}$$

where $\exp(-jm\phi)/T(f)$ represents the steering weight of the m-th phase mode, and $T(f)$ is calculated as:

$$T(f) = \sum_{m=-M}^{M} \sum_{k=1}^{K} \tilde{a}_k(f, 0^\circ) \cdot \exp(jm\varphi_k) \cdot G_m(f), \quad (16)$$

where $\tilde{a}_k(f, 0^\circ)$ is the UCA far-field manifold for the 0° direction, which can be expressed as:

$$\tilde{a}_k(f, 0^\circ) = \exp[j2\pi f \cdot r/c \cdot \cos(0^\circ - \varphi_k)] \cdot \Phi(f, \varphi_k). \quad (17)$$

Note that $T(f)$ in (16) is a generic equation to calculate the normalization coefficient for the UCA gain de-embedding, namely, applicable for both omnidirectional-element-based UCAs and directive-element-based UCAs. After performing inverse discrete Fourier transform (IDFT) to the beam pattern, then we can obtain the power angle delay profile (PADP) $b(\tau, \phi)$.

The beam pattern obtained with the FIBF algorithm has a strong sidelobe for the Omni-VAA [35], which might be mistakenly detected as a path (i.e., fake path) and thereby degrade the channel estimation performance. To eliminate the sidelobe effect, the successive cancellation procedure is adopted, which is detailed in [35] and thereby is only outlined below: we first set the signal threshold value β with respect to the LoS power in decibels. Assuming that we have L paths above the signal threshold, we will have L loops to extract the path parameters and eliminate the sidelobe effect of each path. For the ℓ-th loop to extract the parameter of the ℓ-th path, we perform FIBF to the former frequency response $H_k^{\ell-1}(f)$ and obtain the PADP $b^{\ell-1}(\tau, \phi)$ using IDFT. Then we find the peak amplitude and location of ℓ-th path in the obtained PADP $b(\tau, \phi)$ as:

$$\widehat{\alpha}_\ell = \max_{\alpha} b^{\ell-1}(\tau, \phi), \quad (18)$$

$$\left(\widehat{\tau}_\ell, \widehat{\phi}_\ell\right) = \underset{\tau,\phi}{\operatorname{argmax}}\, b^{\ell-1}(\tau, \phi). \quad (19)$$

Thus, we can synthesize the frequency response of the k-th array element corresponding to the ℓ-th path as:

$$\widehat{H}_k^\ell(f) = \widehat{\alpha}_\ell \exp(-j2\pi f \widehat{\tau}_\ell) \cdot \exp\left[\frac{j2\pi f r \cos\left(\widehat{\phi}_\ell - \varphi_k\right)}{c}\right]. \quad (20)$$

The synthetic CIR $\widehat{\mathbf{h}}^\ell(\tau)$ can be obtained by performing the IDFT to $\widehat{\mathbf{H}}^\ell(f)$, where $\widehat{\mathbf{h}}^\ell(\tau) = [\widehat{h}_1^\ell(\tau); \ldots; \widehat{h}_K^\ell(\tau)]$ and $\widehat{\mathbf{H}}^\ell(f) = [\widehat{H}_1^\ell(\tau); \ldots; \widehat{H}_K^\ell(\tau)]$.

We can remove the ℓ-th path using the following equation:

$$\mathbf{h}^\ell(\tau) = \mathbf{h}^{\ell-1}(\tau) \odot \mathbf{s}(\tau), \quad (21)$$

where $\odot$ denotes the element-wise multiplication, $\mathbf{h}^\ell(\tau) = [h_1^\ell(\tau); \ldots; h_K^\ell(\tau)]$ is the residual of the CIRs of UCA elements. The label vector $\mathbf{s}(\tau) = [s_1(\tau); \ldots; s_K(\tau)]$ is used to remove the contribution of the ℓ-th path in CIRs, where $s_k(\tau)$ for k-th element can be written as:

$$s_k(\tau) = \begin{cases} 0, \tau = \widehat{\tau}_\ell \text{ and } |\widehat{h}_k^\ell(\tau)| > \widehat{\alpha}_1 \cdot 10^{-\beta/20} \\ 1, \text{otherwise} \end{cases}. \quad (22)$$

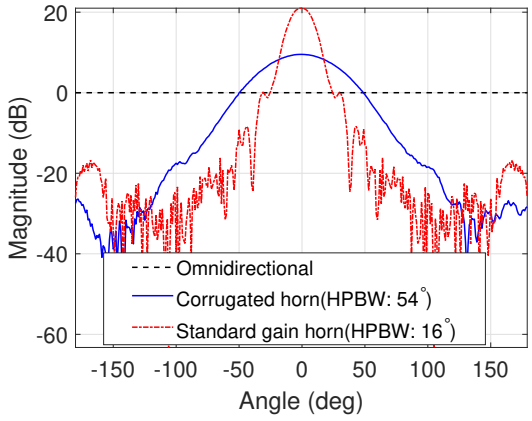

(a)

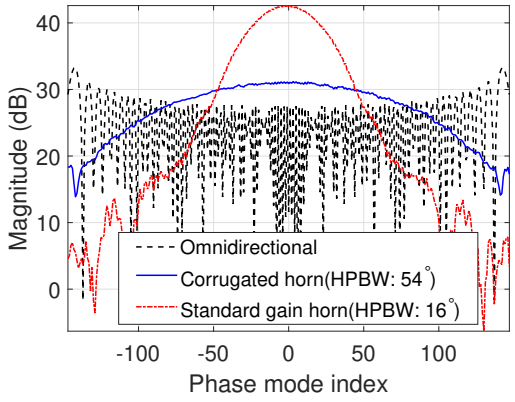

(b)

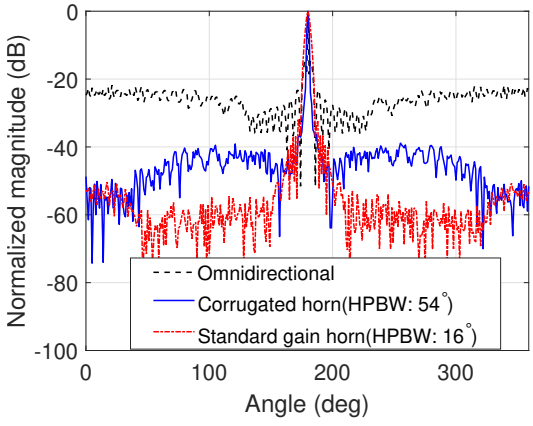

(c)

Fig. 2: Comparison of the array manifold in the phase mode domain for the UCAs composed of elements with different directivity. (a) The element patterns; (b) The array manifolds in the phase mode domain. (c) The array beam patterns.

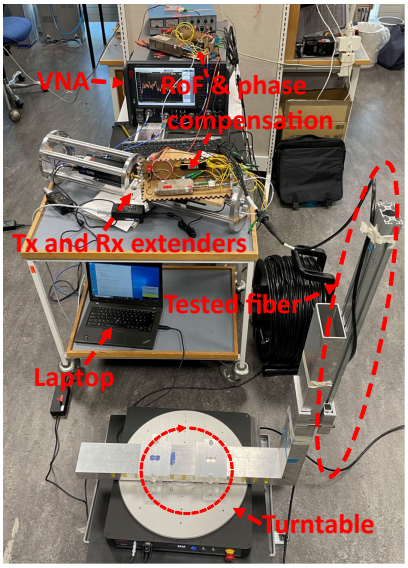

Fig. 3: Photo of the back-to-back measurements using the turntable to mimic the mechanical bending of the fiber.

$\mathbf{h}^{\ell}(\tau)$ is then transformed back to frequency domain as $\mathbf{H}^{\ell}(f)$ for the process in the next loop.

B. Numerical Simulation

A simulation is performed to show the FIBF for a UCA composed of different antennas. The antennas used in the simulation are an omnidirectional antenna with 0 dBi gain, a corrugated horn antenna with a gain of 9.5 dBi and a half-power beamwidth (HPBW) of $54°$, and a standard gain horn antenna with a gain of 20.5 dBi and $16°$ HPBW. The comparison of these three antennas using the extended FIBF algorithm is shown in Fig. 2. It shows that a UCA composed of more directional elements shown in Fig. 2 (a) will lead to a narrower window in the phase mode as shown in Fig. 2 (b). The window will introduce an amplitude tapering effect in the phase domain when performing the extended FIBF. Similar to the amplitude tapering effect in the spatial domain, sidelobe suppression, and main beam broadening will be introduced to the array beam pattern as demonstrated by Fig. 2 (c). Due to the windowing effect in the phase mode domain, we can simply select the phase modes with dominant magnitudes as shown in Fig. 2 (b), resulting in a limited number of phase modes. Hence, for a UCA composed of more directional elements, a smaller mode number can be selected due to the fewer dominant phase modes. The numerical results have demonstrated that our generalized FIBF algorithm works for UCA composed of both omnidirectional and directive antennas.

IV. Back-to-Back Validation

A. Back-to-Back Measurement Validation

The phase instability issue in the VNA-based channel sounder is a key bottleneck for the VAA scheme at the sub-THz band, especially when the RoF scheme is employed. In this section, a back-to-back measurement of the phase-compensated channel sounder is first presented, where the phase instability and its impact on the VAA scheme are demonstrated. A photo of the back-to-back measurements is shown in Fig. 3. Note that the forward link of this channel sounder is similar to the RoF structure in the conventional RoF-enabled VNA-based channel sounders [27], [28], [38]–[41]. The VNA is configured to sweep the frequency range of 75-110 GHz with 1001 frequency points and 500 Hz intermediate frequency (IF) bandwidth. The Tx and Rx antennas are removed, and the Tx and Rx frequency extenders are attached face-to-face in back-to-back measurements. The fiber is mounted on the turntable to mimic the bending of the fiber during the channel measurement using the VAA or DSS scheme. The turntable is set to rotate in an azimuth range of $[0°, 359.5°]$ with a step of $0.5°$, corresponding to 720 virtual array element locations/rotations. The back-to-back measurement took 2 hours, which is close to the actual channel measurements. Before the measurements, a calibration procedure, which performs the normalization procedure in the VNA to set the system response to be 1 for all swept frequency points, is performed for the forward and feedback links. Thus, we can directly measure the amplitude and phase change in the channel sounding system.

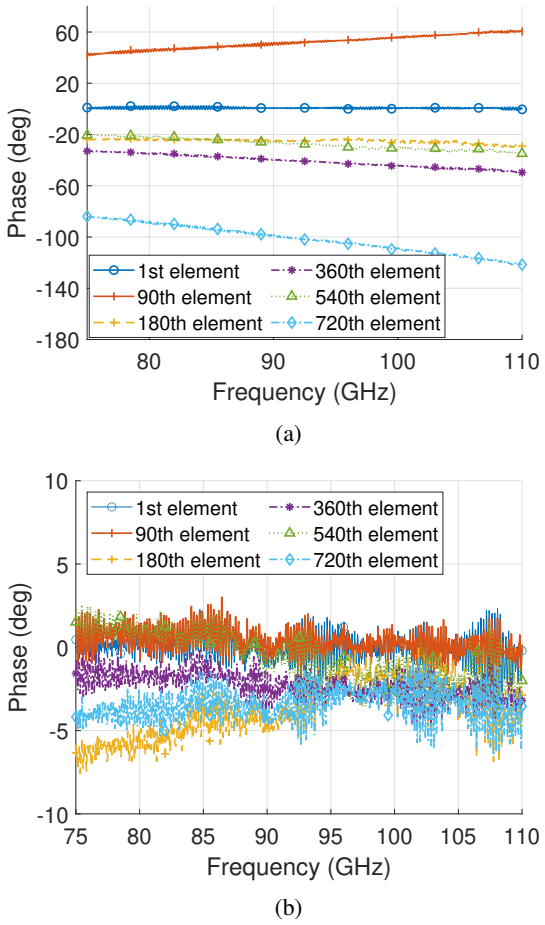

Fig. 4: Phase performance of the phase-compensated channel sounder in back-to-back connection. (a) Forward link. (b) Compensated phase.

TABLE II: The measurement configuration.

Meas. type	Near-field			Long-range		UWB
	Omni-VAA	Dir-VAA	DSS	Omni-VAA	DSS	Omni-VAA
VNA settings						
Frequency range (GHz)	99-101			99-110		
Bandwidth (GHz)	2			11		
Frequency point	1001			7701		
IFBW (Hz)	500					
Transmitted power (dBm)	10					
Antenna settings						
Tx antenna type	Omnidirectional					
Tx antenna gain (dBi)	4.5					
Rx antenna type	Omnidirectional	SGH		Omnidirectional	SGH	Omnidirectional
Rx antenna gain (dBi)	4.5	20		4.5	20	4.5
Rx antenna HPBW (deg)	360	16		360	16	360
Virtual UCA settings						
Radius of the UCA (cm)	6.7		0	6.7	0	6.7
Rotation step (deg)	1					
Number of elements	360					
Scenario settings						
Antenna height (m)	1.3			2.1		1.3
Tx-Rx distance (m)	7.3			84.5		3-58

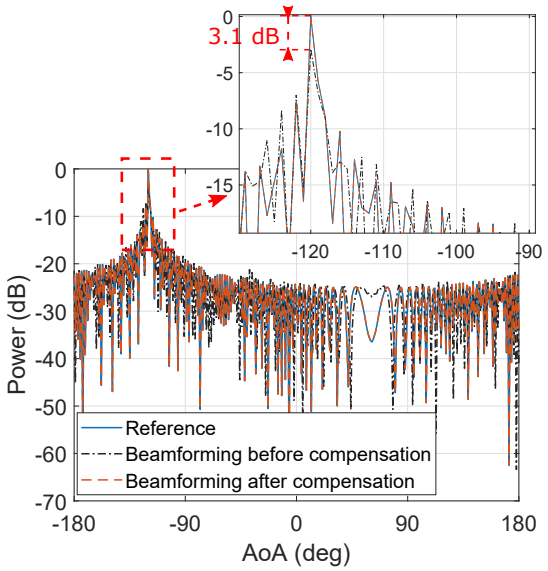

Fig. 5: The comparison of the simulated PAS using the phase before and after the compensation, and the reference PAS.

The phase measurements of the channel sounder of the specified rotations selected from the 720 rotations are depicted in Fig. 4 (a). The phase change caused by the cable bending during the rotation varies from $-121.6°$ to $60.9°$. The feedback response is also measured in the back-to-back measurements, and the compensated phase can be calculated in the post-processing, according to (6). The phase variation after compensation is bounded within $\pm 5°$, as observed in Fig. 4 (b), which demonstrates the effectiveness of the proposed phase compensation scheme.

B. Phase instability on the VAA performance

To demonstrate the impact of the phase instability on the VAA performance, we perform a simulation based on the measured phase values at 100 GHz, where a single path with a magnitude of 0 dB and an angle-of-arrival (AoA) of $-120°$ is set. A 720-element UCA with a radius of 5 cm is simulated, to be consistent with the measurement settings as detailed later. The CFR H_i of the i-th array element at the carrier frequency of $f_c = 100$ GHz is:

$$H_i = \alpha \cdot \exp\left(j2\pi f_c \frac{\vec{\phi} \cdot \vec{r_i}}{c}\right) \exp\left(j\Delta\varphi_i\right), \qquad (23)$$

where α, $\vec{\phi}$, $\vec{r_i}$, and $\Delta\varphi_i$ represent the amplitude, the direction vector of the AoA of the path, the direction vector of the i-th array element, and the measured phase introduced by the fiber in i-th element at the carrier frequency $f_c = 100$ GHz, respectively. The speed of light is denoted as c. Applying the classic beamforming algorithm [31], [36] to the element CFRs with and without phases errors, we can obtain the corresponding power-angle-spectra (PAS) as plotted in Fig. 5, which is a simple and straightforward way to show the impact of the phase change on the channel spatial parameter estimation. It can be observed that peaks of both PASs are located in the preset direction. Though the phase errors do not introduce severe distortion to the beam pattern, they result in a beam peak drop, i.e. 3.1 dB, compared to the reference one, i.e., without phase errors. Similarly, the phase error introduced by the cable effects during the measurements will introduce destructive summation, leading to power loss of the formed beam as well. Note that classical beamforming is the most robust algorithm for phase error. The channel parameter estimations using high-resolution algorithms are typically more susceptible to phase errors. We also perform the same beamforming simulation using the compensated phase, as shown in Fig. 5, where a good agreement with the reference result can be observed.

Compared with the back-to-back measurements, even larger phase errors will present in real over-the-air channel measurement data, due to following reasons:

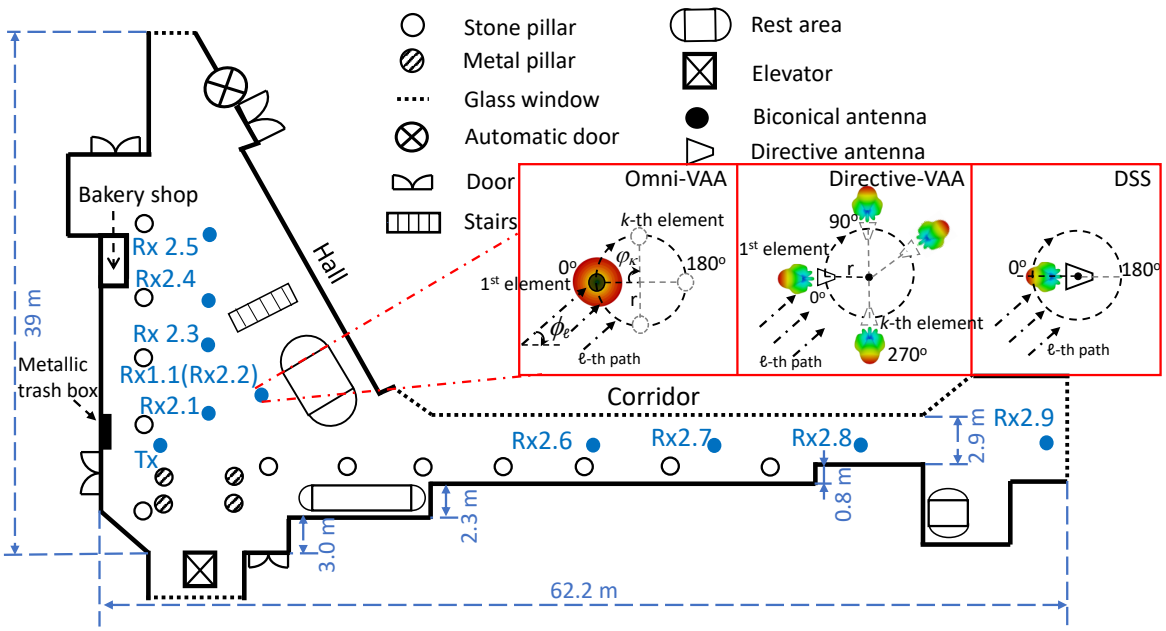

(a)

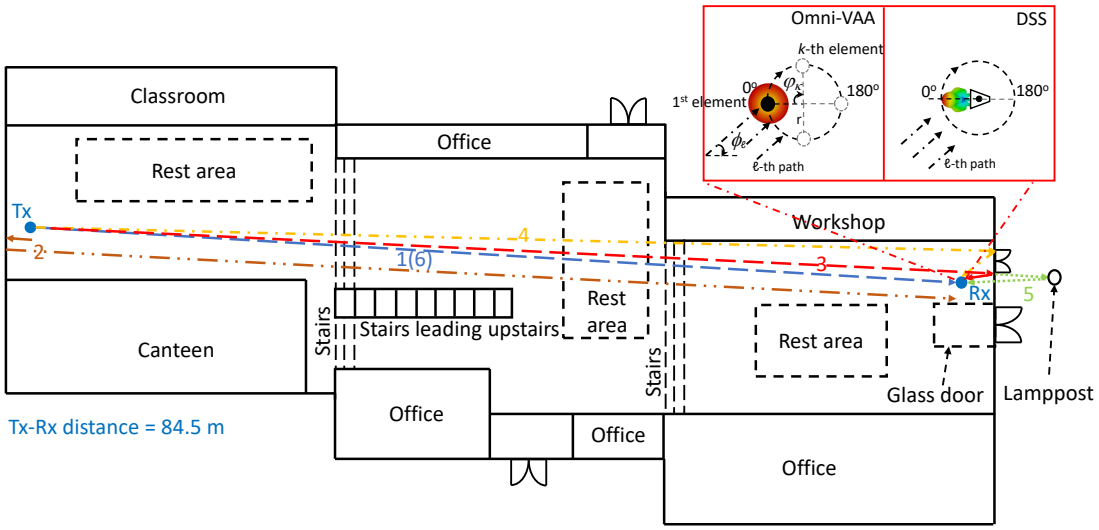

(b)

Fig. 6: Measurement scenario of the VAA at 100 GHz. (a) Near-field and UWB validation. (b) Long-range validation.

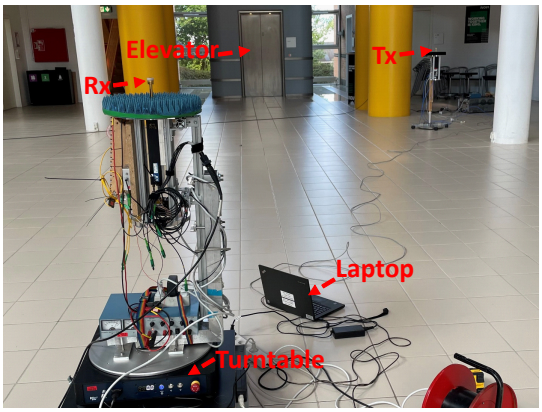

Fig. 7: Photo of the measurement scenario in the near-field case (i.e., Tx-Rx 1.1).

- The positioning errors of VAA elements: In a practical VAA channel sounder, the installment of the antenna, the rotation accuracy, and the stability of the turntable will introduce location errors of VAA elements. For sub-THz frequency bands, the phase will be extremely sensitive to even small positioning errors. For instance, a 1 mm positioning error results in a 120° phase error at 100 GHz.
- Temperature: The VAA measurements often take several hours. The temperature might vary significantly during the measurements, which will introduce large errors.
- Signal condition: In our back-to-back measurements, the signal-to-noise ratio is good, which is too ideal in practice. In over-the-air channel measurements, the signal condition will be much worse, given the signal transmission loss, especially for long-range measurements.

V. Over-the-Air Channel Measurement Validation

In this section, several over-the-air channel measurements are performed to validate the proposed channel sounder as well as the generalized high-resolution channel parameter estimator.

A. Near-field Validation

In this subsection, the Omni-VAA-based channel measurements are conducted to validate our proposed channel sounder and algorithm at sub-THz bands in the near-field case. Note that the Fraunhofer distance of the VAA to distinguish the near- or far-field is

$$d_{\text{far}} = 2D^2/\lambda, \tag{24}$$

where $D = 2R$ denotes the array aperture of the VAA, and λ is the wavelength at the carrier frequency. As stated in Table II, the radius of the VAA R is set to $6.7\,\text{cm}$, which makes the Fraunhofer distance (i.e., far-field distance) for the VAA $12.1\,\text{m}$.

1) Measurement Scenario: The measurement scenario for the near-field case is illustrated in Fig. 6 (a), which contains a spacious hall and a long corridor. The real photo of the scenario is shown in Fig 7. The size of the scenario is $62.2 \times 42\,\text{m}^2$. One side of the corridor has a window with a metallic structure, while on the other side stand seven stone pillars. In the near-field case (i.e., Tx-Rx1.1), the Tx-Rx distance is set to be $7.3\,\text{m}$. which is much smaller than the far-field distance. The VNA is set to sweep in the frequency range of 99-101 GHz with 1001 frequency points, and the IF bandwidth (IFBW) of $500\,\text{Hz}$. The delay resolution is $0.5\,\text{ns}$ (corresponds to the distance resolution of $0.15\,\text{m}$) and the maximum detectable distance is $150\,\text{m}$. An omnidirectional antenna with a gain of $4.5\,\text{dBi}$ [42] is employed as the Tx and Rx antennas to validate the Omni-VAA. Both the Tx and Rx are installed $1.25\,\text{m}$ above the floor. The turntable is set to rotate in the horizontal plane within a range of $[0°, 359°]$ with a step of $1°$ to form a virtual UCA with a radius of $R = 6.7\,\text{cm}$. In addition, DSS-based measurements conducted in the same Tx and Rx locations are taken as references. In the DSS reference measurements, we install a standard gain horn (SGH) antenna with an antenna gain of $20\,\text{dBi}$ and an HPBW of $16°$ [43] at the center of the turntable as the Rx antenna, while keeping the Tx antenna unchanged. Note that before the measurements, we remove the antennas and connect the Tx and Rx waveguides for the back-to-back calibration, i.e., performing the normalization procedure to calibrate the system response. The measurement configurations for the near-field measurements are demonstrated in Table II.

2) Measurement Results: a) DSS result. Fig.8 (a) depicts the PADP result with the DSS in the near-field case. We can identify 10 distinct paths from the PADP. It is obvious that the antenna pattern is embedded in the DSS results, though the paths can be clearly detected in the joint angle and delay domain.

b) Omni-VAA result. Fig. 8 (b) and (c) illustrate the recorded CIR with Omni-VAA and the PADP result with Omni-VAA using the FIBF, respectively. We can also find 10 paths from the recorded CIR. However, with the use of the omnidirectional antenna at the Rx, the dynamic range is found to be lower compared to the PADP with the DSS, as seen in Fig. 8 (b). After the FIBF, a high angular resolution can be observed, though strong sidelobes can be observed, as expected. The LoS path with an AoA of $-33°$ and a delay of $24\,\text{ns}$ (corresponding to the LoS propagation distance of $7.2\,\text{m}$) is estimated in the Tx-Rx 1 case, which matches the distance between the Tx and Rx. According to Friis free-space path loss (FSPL) equation at $100\,\text{GHz}$, we have

$$\text{FSPL} = \ 20 * \log_{10}\left(\frac{4\pi f_c d}{c}\right), \tag{25}$$

where d represents the link distance between the Tx and Rx. The estimated power of the LoS path is $-90.5\,\text{dB}$, which is close to the FSPL ($89.7\,\text{dB}$) calculated in (25) for $d_{\text{LoS}} = 7.3\,\text{m}$. Furthermore, we can observe that the signal-to-noise ratio (SNR) improvement of the PADP after the FIBF compared to the raw CIR (shown in Fig. 8 (b) and

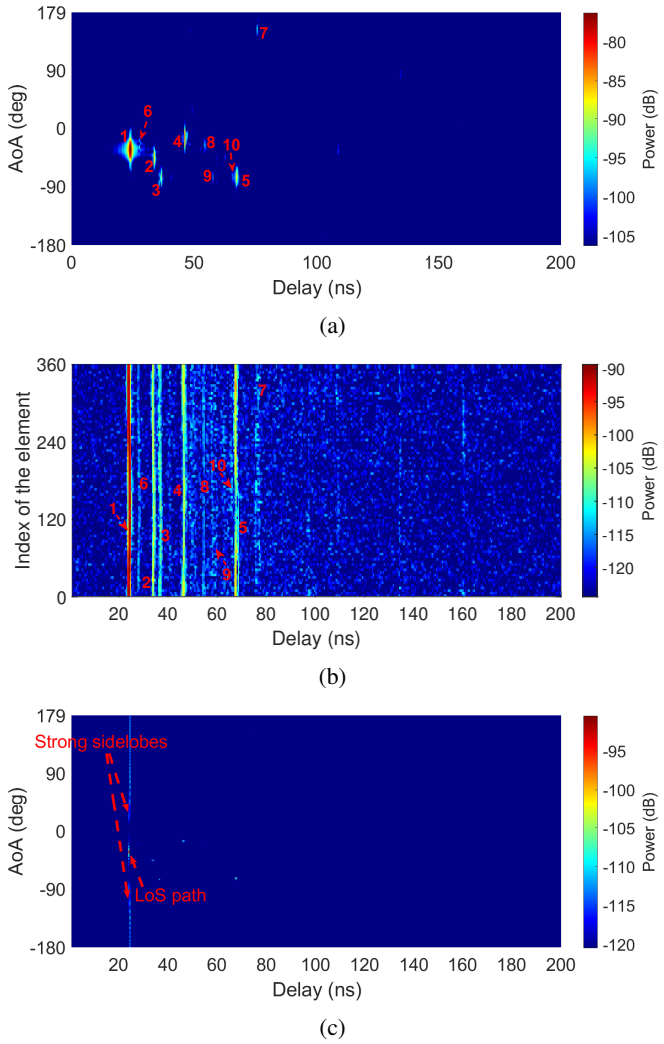

Fig. 8: The measurement results in the near-field case. (a) PADP with the DSS. (b) Recorded CIR with Omni-VAA over array elements. (c) PADP with Omni-VAA with the FIBF method.

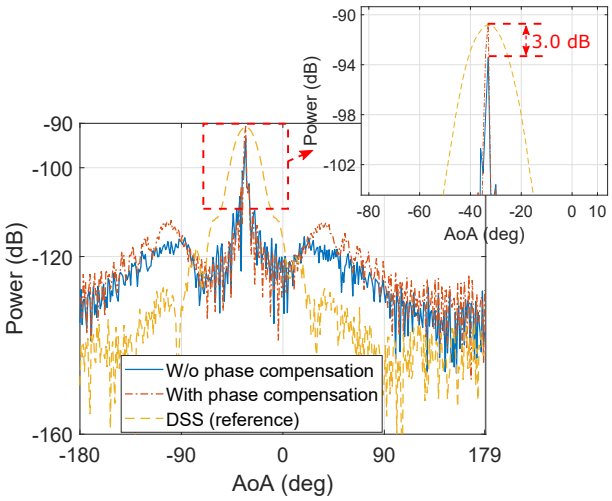

Fig. 9: The exemplary PASs with and without phase compensation after beamforming in comparison with DSS results at the LoS delay ($\tau_{\mathrm{LoS}} = 24\,\mathrm{ns}$) in the near-field case.

Fig. 8 (c)) is 20.5 dB. The theoretical value for the array gain is $10 * \log_{10}(K) = 25.6\,\mathrm{dB}$. The measured array gain is lower than the theoretical one due to measurement non-idealities in the measurement systems, e.g., the correlation between the noise between different elements, near-field propagation, and phase center of the employed horn antenna, etc.

c) LoS path result. To investigate the effectiveness of the phase compensation scheme, the power-angle spectra (PASs) of the LoS path without and with the proposed phase-compensation scheme are extracted by the time-gating technique for a closer look, which is a widely used technique in antenna measurement to filter out multipath components in the measurements. The basic idea is to convert the CFR after the FIBF to CIR using inverse Fourier transform, and then extract the LoS path by a window that filters out delayed multipath components. The resulting PASs are compared with the reference DSS result in Fig. 9. The power of the LoS path after beamforming with phase compensation matches that using the DSS scheme. Besides, comparing the beamforming results with and without phase compensation, the phase errors cause 3.0 dB power drop in the peak, which is consistent with our simulation results presented in Section IV with the synthetic data.

d) Result using the FIBF with the SIC. The FIBF with the SIC procedure is applied to the measured data, where a signal threshold is set to be 10 dB higher than the noise floor. Note that in the following subsection (i.e., long-range and UWB channel validation), the signal thresholds are the same as that in this near-field case. Fig. 10 (a) depicts the estimation results using the FIBF with the SIC. In the near-field case, 10 dominant paths can be detected. The paths are mainly concentrated in the AoA range of $[-90°, 0°]$. Fig. 10 (b) illustrates the paths trajectory. Path 2, 3, 6, and 9 are observed to be the reflections from the pillars. Paths 5 and 10 are the reflections from the elevator. Path 7 is seen to be the reflection from the back wall of the Rx, while paths 4 and 8 are the first-order and second-order reflections from the

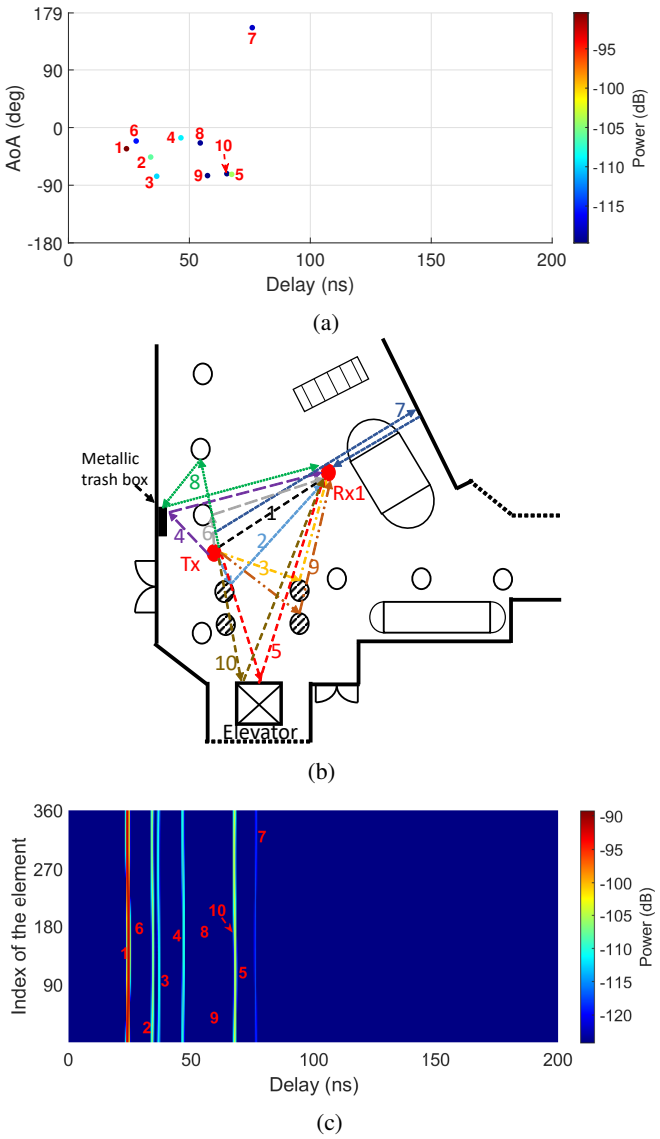

Fig. 10: The estimated results in the near-field case (i.e., Tx-Rx 1.1). (a) Estimated path results. (b) The relation of the detected MPC trajectory to the room geometry. (c) Synthesized CIR using estimated results.

metallic trash box, respectively. The propagation distance and angle of the estimated paths match the geometry of the hall. We also compared the estimation results in Fig. 10 (a) with the DSS results in Fig. 8 (a). The estimation results are found to be well-matched compared to the DSS results. Fig. 10 (c) illustrates the synthesized CIR on the virtual UCA elements using the estimated paths. Compared with the recorded CIR on the virtual UCA elements in Fig. 8 (b), we can observe that most specular paths can be accurately detected.

B. Dir-VAA Validation

In the former near-field subsection, Omni-VAA and DSS measurements are conducted to validate the near-field case. In this subsection, Dir-VAA-based channel measurements are performed in the near-field case (i.e., Tx-Rx1.1) with the

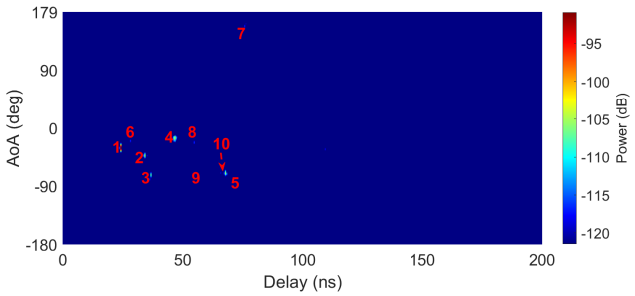

Fig. 11: The PADP results with Dir-VAA after the FIBF.

same Tx-Rx deployment and measurement configurations. Comparing the DSS with Dir-VAA, the measurement system and antenna configurations are the same, the only difference is that the employed directive antenna is centered for the DSS, while off-set with a preset radius for the Dir-VAA of 6.7 cm on the turntable. Comparing the Dir-VAA with Omni-VAA, the only difference is the employed antenna, i.e., the omnidirectional antenna is used as the array element in the Omni-VAA, while the directive antenna is used as the array element in Dir-VAA.

Fig. 11 illustrates the PADP with the Dir-VAA after the FIBF. The LoS power after the FIBF is observed to be -90.9 dB, which is close to the FSPL value. Compared with the DSS PADP in Fig. 8 (c), the distribution of the MPCs is seen to be well-matched. Besides, the angular resolution is significantly improved by the FIBF algorithm (the main beamwidths of the PADP with Dir-VAA after the FIBF and with the DSS are 3° and 16°, respectively). The SNR improvement of the Dir-VAA is 15.0 dB, which is less than that of the Omni-VAA. This phenomenon is reasonable since we use less effective array elements in Dir-VAA compared to Omni-VAA.

The Dir-VAA has a high element gain (20 dBi at 100 GHz in our work) compared to that in the Omni-VAA (4.5 dBi at 100 GHz in our work), which can improve the dynamic range of the channel sounder to support the long-range channel measurements. However, it has a low array gain after beamforming (i.e., 15.0 dB), compared to 20.5 dB array gain in the Omni-VAA in the near-field case, since only the effective array elements are involved. Comparing the Dir-VAA result with the DSS result, a better angular resolution is obtained using the Dir-VAA. However, phase-coherent measurements are required for the Dir-VAA.

C. Long-range Validation

In this subsection, channel measurements are performed to demonstrate that our sounder can support long-range channel measurement. Note that the state-of-the-art long-range measurements generally use directive antennas to improve the system dynamic range, e.g., [27], [28]. In our work, the omnidirectional antennas are intentionally employed for the long-range case to demonstrate the capability of our developed channel sounder.

1) Measurement Scenario: The long-range validation measurements are conducted on the ground floor of Aalborg University (AAU) Innovation Building, as illustrated in Fig. 6 (b).

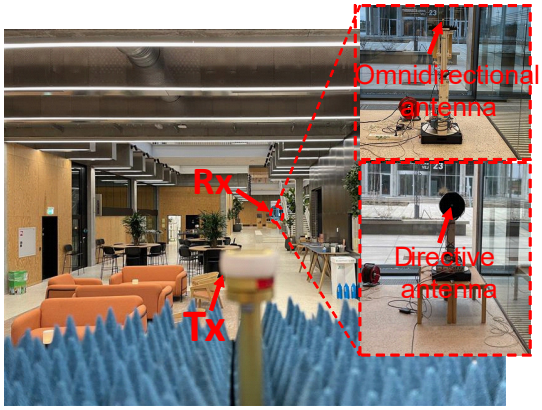

Fig. 12: Photo of the measurement scenario in the long-range case).

The scenario is a typical hall scenario with a size of 94×30 m^2. In this long-range case, the frequency range is set to be 99-110 GHz with a bandwidth of 11 GHz and the number of frequency points of 7701 resulting in a delay (distance) resolution of 0.09 ns (0.03 m) and a maximum measurable distance of 210 m, respectively. The IF bandwidth and transmitted power are 500 Hz and 10 dBm, respectively. Two identical omnidirectional antennas [42] are employed in this case for the Tx and Rx. The Tx-Rx distance is set to be 84.5 m. There is a height difference of 0.73 m between the Tx and Rx due to the stairs between them. To align the antennas, the heights of the Tx and Rx are set as 2.05 m and 1.32 m, respectively. Same to the near-field case, the DSS measurements are also performed as a reference. Fig. 12 and Table II illustrate the photo of the long-range measurement scenario and the measurement configurations, respectively.

2) Measurement Results: Fig.13 (a) depicts the PADP result with the DSS in the long-range case. 6 paths can be detected from the PADP. However, it is hard to detect paths from the recorded CIRs over array elements in Fig.13 (b) due to the low dynamic range of the Omni-VAA in the long-range case. A high angular resolution can be observed after the FIBF, as shown in the PADP after the FIBF in Fig.13 (c). The LoS path has an AoA of 2° and a delay of 281.7 ns (corresponding to the LoS propagation distance of 84.5 m), which matches the deployment distance of the Tx and Rx. The power of the LoS power is -112.9 dB, while the theoretical FSPL value is -111.4 dB. The difference might be due to the fact that the Tx and Rx antennas cannot be preciously aligned over such a long distance. Besides, a strong sidelobe can be seen in Fig.13 (c), as expected for the FIBF algorithm. Moreover, a signal-to-noise ratio (SNR) improvement of the PADP after the FIBF in Fig.13 (c) compared to the raw CIRs in Fig. 13 (b) is 16.0 dB.

Fig. 14 shows the estimated paths and the synthesized CIR on the virtual UCA elements after using the FIBF with the SIC, respectively. Due to the high path loss and the low antenna gain of the employed omnidirectional antennas, we can only detect 6 paths in the measurement results using the FIBF with the SIC. The trajectory of the dominant paths is depicted in Fig. 6 (b). Path 2 is observed as the reflection from

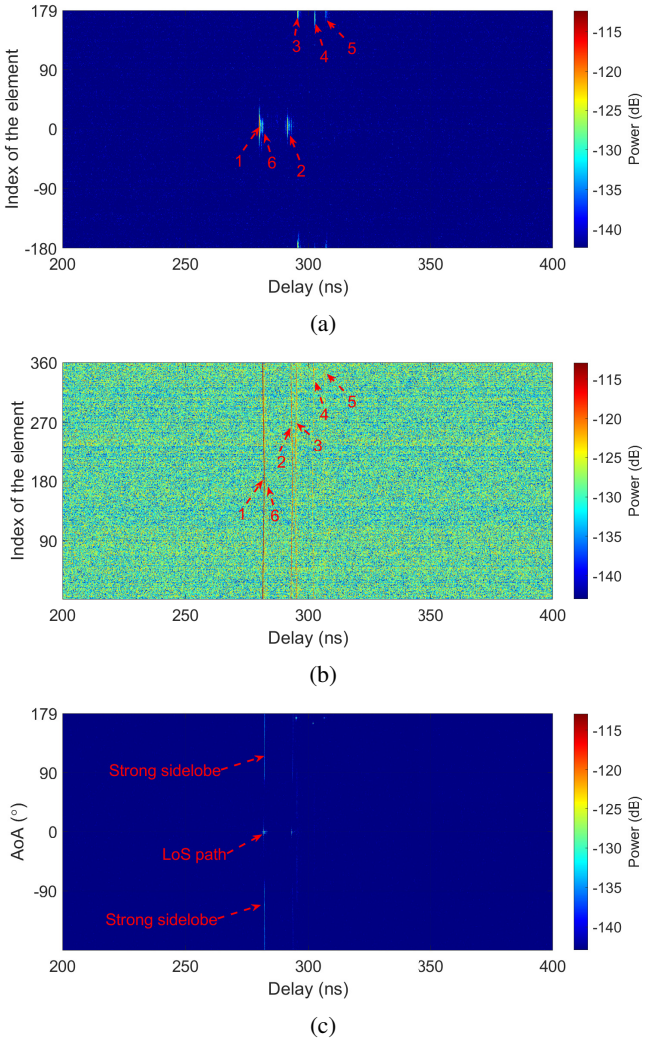

Fig. 13: The measurement results in the long-range case. (a) PADP with the DSS. (b) Recorded CIR with Omni-VAA. (c) PADP with Omni-VAA after the FIBF.

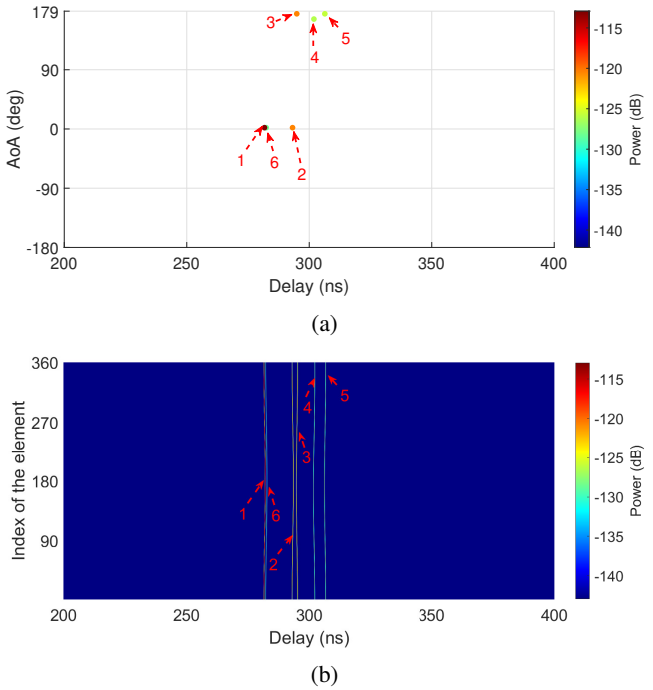

Fig. 14: The estimated results in the near-field case (i.e., Tx-Rx 1.1). (a) Estimated path results. (b) Synthesized CIR using estimated results

the back wall of the Tx, while paths 3 and 4 are seen as the reflection from the metallic structure of the back wall at the Rx side. We observe that path 5 is the reflection from the outdoor lamppost. Path 6 is found to be the reflection from the wooden furniture in the middle rest area. Furthermore, a good agreement can be seen in the comparison of the reconstructed CIR in Fig. 14 (b) with the recorded CIRs over virtual array elements in Fig.13 (b). Besides, the comparison between the estimation results in Fig. 14 (a) and the DSS results in Fig.13 (a) also demonstrates that the dominant paths in these two measurements fit well, validating our measurement results using the VAA concept.

D. UWB Channel Measurements and Characterization

1) Measurement Scenario: The measurement scenario and the Tx and Rx deployments are shown in Fig. 6 (a). We deployed the Tx close to the wall to simulate a base station, while deploying 9 Rx locations (i.e., Rx 2.1-Rx 2.9) with the link distance ranging from 4-58 m. The antenna heights of the Tx and Rx are set the same as 1.25 m. The measurement settings are the same as those in the long-range validation subsection. Thus, we obtained $360 \times 9 = 3240$ CFRs in total (i.e., number of UCA elements $\times$ number of measurement locations). Due to a large number of frequency points and the low IF bandwidth, each measurement takes approximately 4 hours. Therefore, the entire measurements took around 40 hours. The detailed measurement specifications are illustrated in Table II.

2) Channel characterization and modeling: In this subsection, we first use the FIBF with the SIC to extract the parameters (i.e., amplitude, delay, and AoA) of the MPCs for each measurement location, and then calculate the channel characteristics using those estimated channel parameters.

a) Path loss: In this paper, we calculate the path loss (PL) as the power summation of the estimated path power. The calculated path loss results are fitted by the log-distance dependent path loss model, i.e., alpha-beta-gamma (ABG) model [44], [45], which can be written as:

$$PL_{\mathrm{ABG}}(d)[\mathrm{dB}] = 10 \cdot n_{\mathrm{ABG}} \cdot \log_{10}(\frac{d}{d_0}) + PL(d_0) + \chi_{\sigma}^{\mathrm{ABG}} \tag{26}$$

where $PL_{\mathrm{ABG}}(d)$ (in dB) denotes the ABG path loss model over distance. d (in meter) represents the Tx-Rx distance with $d \geq 1\,\mathrm{m}$ and $d_0 = 1\,\mathrm{m}$; n_{ABG} and $PL(d_0)$ are the path loss coefficient and the optimized offset value for path loss, respectively. $\chi_{\sigma}^{\mathrm{ABG}}$ represents the large-scale signal fluctuations.

Fig. 15 depicts the measured path loss compared with the fitted model. Note that we also plot the FSPL model

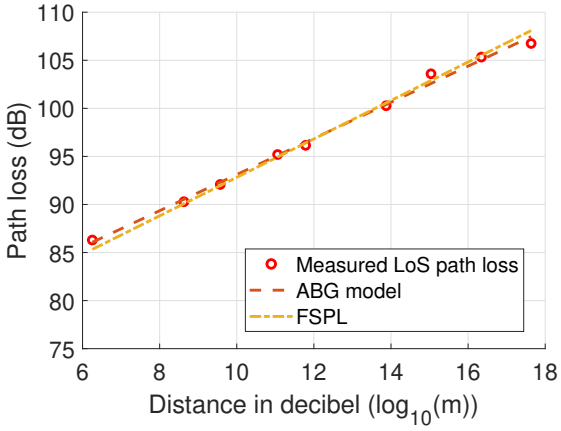

Fig. 15: Element-wise and array-wise omnidirectional PL model at 99-110 GHz compared with the FSPL model.

($\mathrm{PL}_{\mathrm{FSPL}} = 2 \cdot 10 \cdot \log_{10}(d) + 72.82$) in Fig. 15 for reference. Note that the antenna gain is removed from the estimated results before the path loss calculation. The empirical array-wise PL is well-fitted to the ABG path loss model of $\mathrm{PL}_{\mathrm{ABG}} = 1.88 \cdot 10 \cdot \log_{10}(d) + 74.31$ dB with the root-mean-square error (RMSE) of 0.52 dB. The fitted PL model is shown a close agreement with the FSPL model. It is observed that the PL coefficient of the fitted model is smaller than that of the FSPL model. This is due to the fact that the total received signal includes several reflection MPCs in addition to the LoS component, which varies with the Tx-Rx power attenuation due to distance.

b) Delay spread, AoA spread, and k-factor: Delay spread σ_τ and angular spread σ_ϕ are channel parameters to describe the delay and angle span of the MPCs in the channel. Note that the angular spread in this work is referred to as the AoA spread. The Ricean k-factor is a useful parameter for the small-scale channel characterization [46], [47]. Note that we compute and analyze the channel characteristics based on the path parameter estimation results. Readers can refer to [47], [48] for detailed equations to calculate these parameters.

The delay spread is depicted in Fig. 16 (a). The delay spreads vary in the range of $[5.67, 47.61]$ ns, and are seen to be linear with the distance in decibels according to our analysis of the measurement results. Fig. 16 (b) illustrates the AoA spread result. The angular spreads vary from $15.63°$ to $72.11°$ in this scenario. This scenario can be separated into two cases, i.e., spacious hall (Rx 2.1-2.5) and corridor (Rx 2.6-2.9). The AoA spreads are observed to increase with the Tx-Rx distance in both cases, as shown in Fig. 16 (b). The exemplary PASs with the estimated results compared with the mean AoA $\hat{\phi}_\ell$ in the Tx-Rx2.2 and Tx-Rx2.9 are depicted in Fig. 17. It can be observed that the MPCs in Tx-Rx2.2 are concentrated on the mean angle, which leads to a low AoA spread. While in Tx-Rx2.9, the AoAs of the MPCs vary from $[-123, 180]°$, which leads to a high angular spread. The k-factor is observed to decrease with increasing distance. These observations are as expected due to the fact that as the distance increases, the LoS power decreases and the power of the MPC becomes

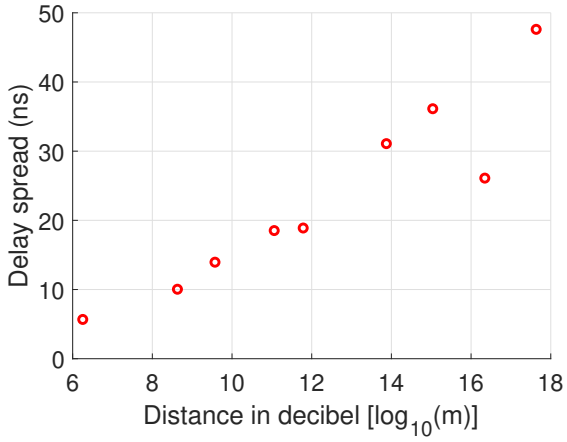

(a)

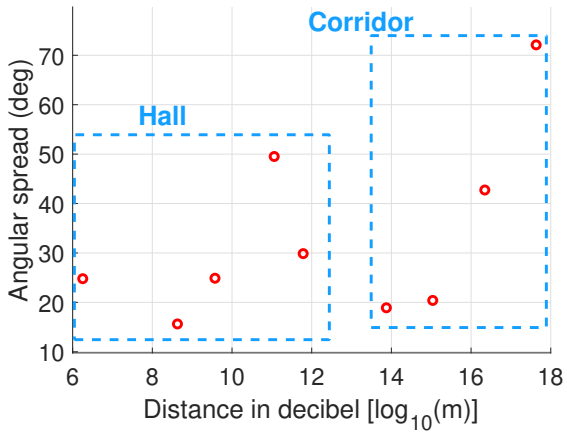

(b)

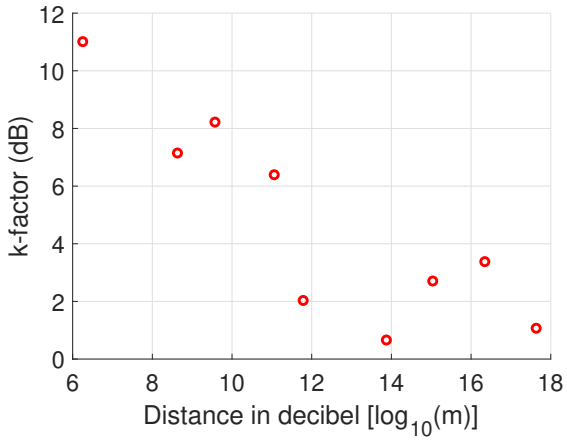

(c)

Fig. 16: Channel parameters with the Tx-Rx distance. (a) Delay spread; (b) angular spread; (c) k-factor.

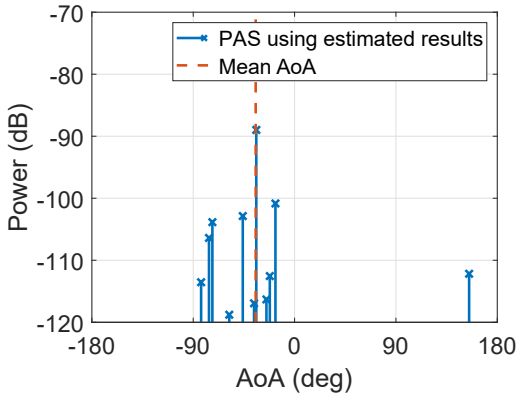

(a)

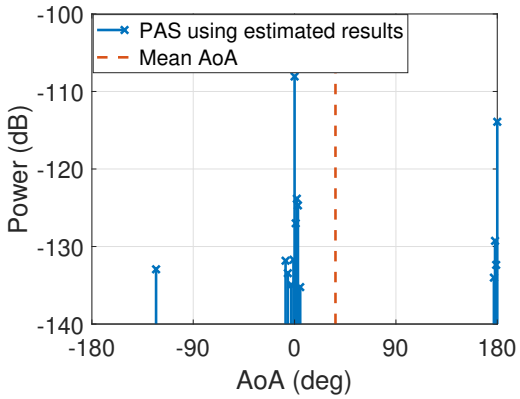

(b)

Fig. 17: The exemplary comparison of the PAS with estimated results and the mean AoA. (a) Tx-Rx2.2. (b)Tx-Rx2.9.

comparable to the LoS power, which can be also observed from the comparison of the power of the MPCs between the Tx-Rx2.2 and Tx-Rx2.9 in Fig. 17.

VI. Conclusion

This paper presents the design, implementation, and validation of a phase-compensated channel sounder that can support the VAA scheme and long-range measurements at W bands (i.e., 75-110 GHz). The phase stability becomes a critical issue at sub-THz bands due to the unstable phase performance of the channel sounder in state-of-the-art channel sounder, making it inapplicable for applying advanced array signal processing algorithms to extract channel path parameters. According to the simulation, the VAA scheme cannot be directly employed in the conventional sub-THz channel sounder, since the unstable phase performance might lead to beamforming gain loss up to 3.1 dB, even in the ideal back-to-back measurements. With the help of the phase compensation scheme, this issue can be effectively addressed, where a phase variation up to $\pm 5^{\circ}$ can be achieved in the back-to-back connection in the W-band. Virtual UCA-based channel measurements in two cases, i.e., near-field (with an LoS distance of 7.3 m) and long-range (with an LoS distance of 84.5 m) cases, are performed at 100 GHz to validate the proposed channel sounder, where a high-resolution channel parameter estimator, i.e., FIBF with the SIC, is applied to extract the MPC parameters. The focus of the near-field case is to validate the generalized high-resolution channel parameter estimator, while in the long-range case, we aim to demonstrate the capability of our proposed channel sounder with a large dynamic range via intentionally employing omnidirectional antennas on both the Tx and Rx sides and setting the Tx-Rx distance to 84.5 m. In the long-range cases, 6 specular paths are observed including only the LoS path and the first-order reflections, while in the near-field case, approximately 10 paths are identified including the LoS path and the first-order reflections, as well as several second-order reflections. Both measurement results demonstrate the sparse property of the W-band channel. We also perform the reference measurements using the conventional DSS to validate the estimated path parameters. Compared to the DSS results, consistent path parameters in terms of path power, angle, and delay are obtained using the FIBF with the SIC for both cases. These extracted path parameters are utilized to reconstruct the CIRs over the UCA elements. The comparison between the reconstructed CIR and the recorded CIR demonstrates a high level of concordance. Besides, the FIBF algorithm is also extended to a more generic algorithm, which can work for far/near-field, wideband/narrowband propagation scenarios using Omni-VAA and Dir-VAA. Furthermore, Omni-VAA-based UWB measurement validation in the frequency range of [99,110] GHz is performed in a hall scenario at 9 different Rx locations covering the link distance of [3,58] m. Applying the FIBF with the SIC algorithm, the power, delay, and AoA of the MPCs are extracted from the measurement results. In addition, the basic channel characteristics, i.e., path loss, delay spread, angular spread, and k-factor, are analyzed and presented.

Acknowledgement

The authors would like to thank Yifa Li, Sigurd Sándor Petersen, and Kim Olesen for their help with the measurements. The work was partially supported by the 21NRM03 MEWS project, which has received funding from the European Partnership on Metrology, co-financed from the European Union's Horizon Europe Research and Innovation Programme, and by the Participating States.

References

[1] T. S. Rappaport, Y. Xing, O. Kanhere, S. Ju, A. Madanayake, S. Mandal, A. Alkhateeb, and G. C. Trichopoulos, "Wireless communications and applications above 100 GHz: Opportunities and challenges for 6G and beyond," *IEEE Access*, vol. 7, pp. 78 729–78 757, 2019.

[2] Z. Ma, B. Ai, R. He, Z. Zhong, and M. Yang, "A non-stationary geometry-based MIMO channel model for millimeter-wave UAV networks," *IEEE Journal on Selected Areas in Communications*, vol. 39, no. 10, pp. 2960–2974, 2021.

[3] I. F. Akyildiz, C. Han, Z. Hu, S. Nie, and J. M. Jornet, "Terahertz band communication: An old problem revisited and research directions for the next decade," *IEEE Trans. Commun.*, vol. 70, no. 6, pp. 4250–4285, 2022.

[4] K. Guan, H. Yi, D. He, B. Ai, and Z. Zhong, "Towards 6G: Paradigm of realistic terahertz channel modeling," *China Commun.*, vol. 18, no. 5, pp. 1–18, 2021.

[5] C. Han, Y. Wang, Y. Li, Y. Chen, N. A. Abbasi, T. Kürner, and A. F. Molisch, "Terahertz wireless channels: A holistic survey on measurement, modeling, and analysis," *IEEE Communications Surveys & Tutorials*, vol. 24, no. 3, pp. 1670–1707, 2022.

[6] FCC, "FCC opens spectrum horizons for new services and technologies," Mar. 2019. [Online]. Available: https://www.fcc.gov/document/fcc-opens-spectrum-horizons-new-services-technologies

[7] M. J. Marcus, "WRC-19 issues: Agenda item 1.15 and the use of 275 - 450 GHz," *IEEE Wireless Communications*, vol. 23, no. 6, pp. 2–3, 2016.

[8] A. Pärssinen, M.-S. Alouini, M. Berg, T. Kürner, P. Kyösti, M. E. Leinonen, M. Matinmikko-Blue, E. McCune, U. Pfeiffer, and P. Wambacq, "White paper on RF enabling 6G – opportunities and challenges from technology to spectrum," *6G Flagship Ecosystem*, Apr. 2021. [Online]. Available: https://www.6gchannel.com/items/6g-white-paper-rf-spectrum/

[9] J. Huang, C. Wang, R. Feng, J. Sun, W. Zhang, and Y. Yang, "Multi-frequency mmwave massive MIMO channel measurements and characterization for 5G wireless communication systems," *IEEE Journal on Selected Areas in Communications*, vol. 35, no. 7, pp. 1591–1605, 2017.

[10] D. K. Ghodgaonkar, V. V. Varadan, and V. K. Varadan, "A free-space method for measurement of dielectric constants and loss tangents at microwave frequencies," *IEEE Transactions on Instrumentation and Measurement*, vol. 38, no. 3, pp. 789–793, June 1989.

[11] T. Dammes, W. Endemann, and R. Kays, "Frequency domain channel measurements for wireless localization - practical considerations and effects of the measurement," in *European Wireless 2012; 18th European Wireless Conference 2012*, 2012, pp. 1–8.

[12] M. Hiebel, "Fundamentals of vector network analysis," *Microwaves and RF*, vol. 46, no. 10, p. 70, 10 2007.

[13] Y. Lyu, A. W. Mbugua, K. Olesen, P. Kyösti, and W. Fan, "Design and validation of the phase-compensated long-range sub-THz VNA-based channel sounder," *IEEE Antennas and Wireless Propagation Letters*, pp. 1–1, 2021.

[14] J. Medbo, H. Asplund, J.-E. Berg, and N. Jalden, "Directional channel characteristics in elevation and azimuth at an urban macrocell base station," in *Proc. 6th Eur. Conf. Antennas Propag. (EuCAP)*, 2012, pp. 428–432.

[15] C. Gentile, S. M. Lopez, and A. Kik, "A comprehensive spatial-temporal channel propagation model for the ultrawideband spectrum 2 - 8 GHz," *IEEE Trans. Antennas Propagat.*, vol. 58, no. 6, pp. 2069–2077, 2010.

[16] T. Zhou, C. Tao, S. Salous, and L. Liu, "Measurements and analysis of angular characteristics and spatial correlation for high-speed railway channels," *IEEE Transactions on Intelligent Transportation Systems*, vol. 19, no. 2, pp. 357–367, 2018.

[17] C. Gustafson, K. Haneda, S. Wyne, and F. Tufvesson, "On mm-wave multipath clustering and channel modeling," *IEEE Trans. Antennas Propagat.*, vol. 62, no. 3, pp. 1445–1455, 2014.

[18] J. Medbo, H. Asplund, and J.-E. Berg, "60 GHz channel directional characterization using extreme size virtual antenna array," in *2015 IEEE 26th Annual International Symposium on Personal, Indoor, and Mobile Radio Communications (PIMRC)*, 2015, pp. 176–180.

[19] H.-A. Nguyen, W. Keusgen, and T. Eichler, "Instantaneous direction of arrival measurements in mobile radio channels using virtual circular array antennas," in *2016 IEEE Globecom Workshops (GC Wkshps)*, 2016, pp. 1–7.

[20] A. Mudonhi, R. D'Errico, and C. Oestges, "Indoor mmwave channel characterization with large virtual antenna arrays," in *Proc. 14th Eur. Conf. Antennas Propag. (EuCAP)*, 2020, pp. 1–5.

[21] J. Hong, J. Rodríguez-Piñeiro, X. Yin, and Z. Yu, "Joint channel parameter estimation and scatterers localization," *IEEE Transactions on Wireless Communications*, pp. 1–1, 2022.

[22] D. Guven, B. F. Jamroz, J. Chuang, C. Gentile, R. D. Horansky, K. A. Remley, D. F. Williams, J. T. Quimby, A. J. Weiss, and R. Leonhardt, "Methodology for measuring the frequency dependence of multipath channels across the millimeter-wave spectrum," *IEEE Open Journal of Antennas and Propagation*, vol. 3, pp. 461–474, 2022.

[23] U. T. Virk, L. Hentilä, P. Kyösti, and J. Kyröläinen, "Validating FR2 MIMO OTA channel models in 3D MPAC," in *2022 16th European Conference on Antennas and Propagation (EuCAP)*, 2022, pp. 01–05.

[24] A. W. Mbugua, W. Fan, K. Olesen, X. Cai, and G. F. Pedersen, "Phase-compensated optical fiber-based ultrawideband channel sounder," *IEEE Trans. Microw. Theory Techn.*, vol. 68, no. 2, pp. 636–647, 2020.

[25] M. Li, F. Zhang, X. Zhang, Y. Lyu, and W. Fan, "Omni-directional pathloss measurement based on virtual antenna array with directional antennas," *IEEE Transactions on Vehicular Technology*, pp. 1–5, 2022.

[26] Y. Lyu, Z. Yuan, M. Li, A. Mbugua, P. Kyösti, and W. Fan, "Enabling long-range large-scale channel sounding at sub-thz bands: Virtual array and radio-over-fiber concepts," *IEEE Communications Magazine*, Nov. 2022.

[27] S. L. H. Nguyen, J. Järveläinen, A. Karttunen, K. Haneda, and J. Putkonen, "Comparing radio propagation channels between 28 and 140 GHz bands in a shopping mall," in *12th European Conference on Antennas and Propagation (EuCAP 2018)*, 2018, pp. 1–5.

[28] N. A. Abbasi, A. Hariharan, A. M. Nair, A. S. Almaiman, F. B. Rottenberg, A. E. Willner, and A. F. Molisch, "Double directional channel measurements for THz communications in an urban environment," in *ICC 2020 - 2020 IEEE International Conference on Communications (ICC)*, 2020, pp. 1–6.

[29] Y. Xing and T. S. Rappaport, "Propagation measurements and path loss models for sub-THz in urban microcells," in *ICC 2021 - IEEE International Conference on Communications*, 2021, pp. 1–6.

[30] A. Molisch, *Wireless communications.* John Wiley & Sons Ltd., 2011.

[31] A. W. Mbugua, W. Fan, Y. Ji, and G. F. Pedersen, "Millimeter wave multi-user performance evaluation based on measured channels with virtual antenna array channel sounder," *IEEE Access*, vol. 6, pp. 12 318–12 326, 2018.

[32] W. Fan, A. W. Mbugua, and K. Olesen, "Accurate channel sounding with a phase stabilizing scheme," in *2020 XXXIIIrd General Assembly and Scientific Symposium of the International Union of Radio Science*, 2020, pp. 1–4.

[33] J. Noda, K. Okamoto, and Y. Sasaki, "Polarization-maintaining fibers and their applications," *Journal of Lightwave Technology*, vol. 4, no. 8, pp. 1071–1089, 1986.

[34] V. Budinski and D. Donlagic, "Fiber-optic sensors for measurements of torsion, twist and rotation: A review," *Sensors*, vol. 17, no. 3, 2017.

[35] F. Zhang and W. Fan, "Near-field ultra-wideband mmwave channel characterization using successive cancellation beamspace UCA algorithm," *IEEE Transactions on Vehicular Technology*, vol. 68, no. 8, pp. 7248–7259, 2019.

[36] H. Krim and M. Viberg, "Two decades of array signal processing research: the parametric approach," *IEEE Signal Processing Magazine*, vol. 13, no. 4, pp. 67–94, 1996.

[37] Z. Yuan, J. Zhang, Y. Ji, G. F. Pedersen, and W. Fan, "Spatial non-stationary near-field channel modeling and validation for massive mimo systems," *IEEE Transactions on Antennas and Propagation*, pp. 1–1, 2022.

[38] T. Niiho, M. Nakaso, K. Masuda, H. Sasai, K. Utsumi, and M. Fuse, "Multi-channel wireless LAN distributed antenna system based on radio-over-fiber techniques," in *The 17th Annual Meeting of the IEEELasers and Electro-Optics Society, 2004. LEOS 2004.*, vol. 1, 2004, pp. 57–58 Vol.1.

[39] R. Sambaraju, K. Harrison, J. George, A. Ng'Oma, and C.-T. Lin, "Impact of channel characteristics on the performance of a 60 GHz radio over fiber (RoF) system," in *2011 International Topical Meeting on Microwave Photonics jointly held with the 2011 Asia-Pacific Microwave Photonics Conference*, 2011, pp. 157–160.

[40] I. Oppermann, J. Talvitie, and D. Hunter, "Wide-band wireless local loop channel for urban and sub-urban environments at 2 GHz," in *Proceedings of ICC'97 - International Conference on Communications*, vol. 1, 1997, pp. 61–65 vol.1.

[41] L. Tarlazzi, P. Faccin, E. M. Vitucci, F. Fuschini, and V. Degli-Esposti, "Characterization of an interleaved F-DAS MIMO indoor propagation channel," in *2010 Loughborough Antennas & Propagation Conference*, 2010, pp. 505–508.

[42] "W-band omnidirectional antenna." [Online]. Available: https://sftp.eravant.com/content/datasheets/SAO-7531140230-10-S1.pdf

[43] "Flann standrad gain horn antenna 27240-20." [Online]. Available: https://flann.com/products/antennas/standard-gain-horns-series-240/

[44] T. S. Rappaport, G. R. MacCartney, M. K. Samimi, and S. Sun, "Wide-band millimeter-wave propagation measurements and channel models for future wireless communication system design," *IEEE Transactions on Communications*, vol. 63, no. 9, pp. 3029–3056, 2015.

[45] K. Haneda, N. Omaki, T. Imai, L. Raschkowski, M. Peter, and A. Roivainen, "Frequency-agile pathloss models for urban street canyons," *IEEE Transactions on Antennas and Propagation*, vol. 64, no. 5, pp. 1941–1951, 2016.

[46] L. Greenstein, D. Michelson, and V. Erceg, "Moment-method estimation of the ricean k-factor," *IEEE Communications Letters*, vol. 3, no. 6, pp. 175–176, 1999.

[47] N. A. Abbasi, J. L. Gomez, R. Kondaveti, S. M. Shaikbepari, S. Rao, S. Abu-Surra, G. Xu, J. Zhang, and A. F. Molisch, "THz band channel measurements and statistical modeling for urban D2D environments," *IEEE Transactions on Wireless Communications*, vol. 22, no. 3, pp. 1466–1479, 2023.

[48] C. Ling, X. Yin, R. Müller, S. Häfner, D. Dupleich, C. Schneider, J. Luo, H. Yan, and R. Thomä, "Double-directional dual-polarimetric

cluster-based characterization of 70–77 ghz indoor channels," *IEEE Transactions on Antennas and Propagation*, vol. 66, no. 2, pp. 857–870, 2018.

Yejian Lyu received the B.Sc and M.Sc degrees in electric engineering from Tongji University, Shanghai, China, in 2017 and 2020, respectively. He is currently pursuing the Ph.D. degree with the Antennas, Propagation, and Millimeter-wave Systems (APMS) Section, Aalborg University, Aalborg, Denmark. His main research interests include mmWave and sub-THz channel sounding, parameter estimation, and modeling.

Zhiqiang Yuan received the B.S. degree from Beijing University of Posts and Telecommunications (BUPT) in 2018, and has been pursuing the Ph.D. degree in BUPT since 2020. He is also a visiting Ph.D. student in the Antennas, Propagation, and Millimeter-wave systems (APMS) section, Aalborg University, Denmark, from 2021. He currently focuses on research of channel sounding and modeling for massive MIMO systems, channel parameter estimation algorithms, and channel sounding and modeling at mmWave and sub-THz bands.

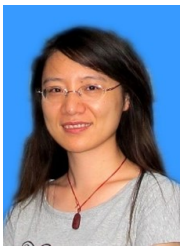

Fengchun Zhang received her B.Sc. degree in optical information science and technology, and the M. Sc. in acoustics from the South China University of Technology, Guangzhou, China, in 2006 and 2009, respectively. She received her Ph.D degree from Aalborg University, Denmark in 2019. She is currently Assistant Professor with the Department of Electronics Systems, Aalborg University, Denmark. Her research interests are in antenna array signal processing, beamforming, parameter estimation for channel characterization of centimeter and millimeter wave wireless systems, and over-the-air testing.

Pekka Kyösti received the M.Sc. degree in mathematics from the University of Oulu, Oulu, Finland. From 1998 to 2002, he was with Nokia Networks, Oulu. From 2002 to 2016, he was with Elektrobit/Anite, Oulu. Since 2002, he has been involved in radio channel measurements, estimation, and modeling. From 2008 to 2012, he actively developed methods for MIMO over-the-air testing. He was moved to Keysight Technologies Finland Oy, Oulu, along with the acquisition in 2016, where he is currently involved in channel modeling for 5G systems and is also currently with the Centre for Wireless Communications, University of Oulu.

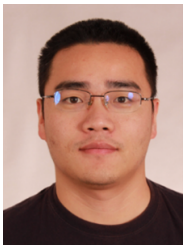

Wei Fan (Senior Member, IEEE) received the B.E. degree from the Harbin Institute of Technology, Harbin, China, in 2009, the double master's degree (Hons.) from the Politecnico di Torino, Turin, Italy, and the Grenoble Institute of Technology, Grenoble, France, in 2011, and the Ph.D. degree from Aalborg University, Aalborg, Denmark, in 2014. Since 2014, he has been with Aalborg University, where he became an Assistant Professor in 2014, a tenured associate professor, and Leader of the "wireless propagation and over-the-air (OTA) testing" research group in 2017 and was admitted to the Professor promotion program in 2023. He was with Intel Mobile Communications, Denmark in 2011 and with Anite Telecoms Oy (now Keysight technologies), Finland in 2014 as a research intern. He also holds a Docentship (adjunct professor) with Oulu University, Finland since 2023. He was the recipient of the Sapere Aude research talent award from Independent Research Fund Denmark in 2016, URSI Young Scientist Award in 2018 and 2020, IEEE AP-S Young Professional Ambassador in 2023, and an unrestricted research gift award from Meta platforms, USA in 2023. His current research interests include over-the-air (OTA) testing of multiple antenna systems, radio channel sounding, parameter estimation, modeling, and emulation.